ADVANCED FUNCTIONAL MATERIALS
www.afm-journal.de

Ultrasensitive Solar-Blind Ultraviolet Photodetector Based on $FePSe_3/MoS_2$ Heterostructure Response to 10.6 µm

Mingsheng Long, Zhen Shen, Ruijie Wang, Qingsong Dong, Zhiyi Liu, Xin Hu, Jie Hou, Yuan Lu, Fang Wang,* Dongxu Zhao, Fei Ding, Yubing Tu, Tao Han, Feng Li, Zongyuan Zhang, Xingyuan Hou, Shaoliang Wang, and Lei Shan**

Metal phosphorous tri-chalcogenides are a category of new ternary 2D layered materials with a wide range of tuneable bandgaps (1.2–3.5 eV). These wide-bandgap semiconductors exhibit great potential applications in solar-blind ultraviolet (SBUV) photodetection. However, these 2D solar-blind photodetectors suffer from low photoresponsivity, slow photoresponse speed, and narrow operation spectral region, thereby limiting their practical applications. Here, an ultra-broadband photodetection based on a $FePSe_3/MoS_2$ heterostructure with coverage ranging from solar-blind ultraviolet 265 nm to longwave infrared (LWIR) 10.6 µm is reported. Notably, the device exhibits excellent weak light detection capability. A high photoresponsivity of 33 600 A W^{-1} and an external quantum efficiency of 1.57×10^7% are demonstrated. A noise-equivalent power as low as 5.7×10^{-16} W $Hz^{-1/2}$ and a specific detectivity up to 1.51×10^{13} cm $Hz^{1/2}$ W^{-1} are realized in the SBUV region. The room temperature LWIR photoresponsivity of 0.12 A W^{-1} is realized. This work opens a route to design high-performance SBUV photodetectors and wide spectral photoresponse applications.

1. Introduction

The discovery of metal phosphorous tri-chalcogenides (MPX_3, with M transition metal, X = S, Se, Te) has attracted widespread research interest both in fundamental understanding and device applications due to its wide tune bandgap of 1.2-3.5 eV.[1,2] MPX_3, which has a larger bandgap than transition metal dichalcogenides (TMDs) of 1.0–2.0 eV,[3] is a promising candidate for ultraviolet (UV) detectors. UV radiation refers to the wavelength of the spectrum ranging from 10 to 400 nm, which constitutes 10% of the total solar spectrum.[4] Due to the absorption of the atmosphere, UV radiation with a wavelength below 280 nm of the sunlight cannot reach the surface of the earth (solar-blind), which has been completely absorbed by the ozone layer. Photodetectors operating in the SBUV spectral range (200–280 nm) on Earth have high signal-to-noise ratios without background radiation, which has been widely applied in missile plume tracking, flame detection, missile early warning, and secure optical communication. UV detectors based on $MnPS_3$ (3.0 eV),[5] $MnPSe_3$ (2.3 eV)[6] $NiPS_3$ (1.6 eV),[7] $FePS_3$ (1.5 eV),[8] $Ga_2In_4S_9$,[9] and $Sr_2Nb_3O_{10}$[10] were demonstrated. However, the study of SBUV photodetectors based on MPX_3 remains elusive. To date, state-of-the-art SBVU photodetectors based on wide-bandgap semiconductors (WBS), such as GaN,[11] ZnO,[12] SiC,[13] Ga_2O_3,[14] and, most recently, 2D WBS, including BiOCl,[15,16] KNb_3O_8,[17] CuBr,[18] and H-BN,[19] have been developed. $FePSe_3$ is a *p*-type

M. Long, Z. Shen, R. Wang, Q. Dong, Z. Liu, X. Hu, J. Hou, Y. Tu, T. Han, F. Li, Z. Zhang, X. Hou, S. Wang, L. Shan
Information Materials and Intelligent Sensing Laboratory of Anhui Province
Key Laboratory of Structure and Functional Regulation of Hybrid Materials of Ministry of Education
Institutes of Physical Science and Information Technology
Anhui University
111 Jiu Long Road, Hefei 230601, China
E-mail: longms@ahu.edu.cn; lshan@ahu.edu.cn

Y. Lu
Infrared and Low-Temperature Plasma Key Laboratory of Anhui Province
State Key Laboratory of Pulsed Power Laser Technology
NUDT
460 Huangshan Road, Hefei 230037, China

The ORCID identification number(s) for the author(s) of this article can be found under https://doi.org/10.1002/adfm.202204230.

F. Wang
State Key Laboratory of Infrared Physics
Shanghai Institute of Technical Physics
Chinese Academy of Sciences
500 Yu Tian Road, Shanghai 200083, China
E-mail: fwang@mail.sitp.ac.cn

D. Zhao
State Key Laboratory of Luminescence and Applications
Changchun Institute of Optics
Fine Mechanics and Physics
Chinese Academy of Sciences
3888 Dongnanhu Road, Changchun 130033, China

F. Ding
Institut für Festkörperphysik
Leibniz Universität Hannover
Appelstraße 2, 30167 Hannover, Germany

DOI: 10.1002/adfm.202204230

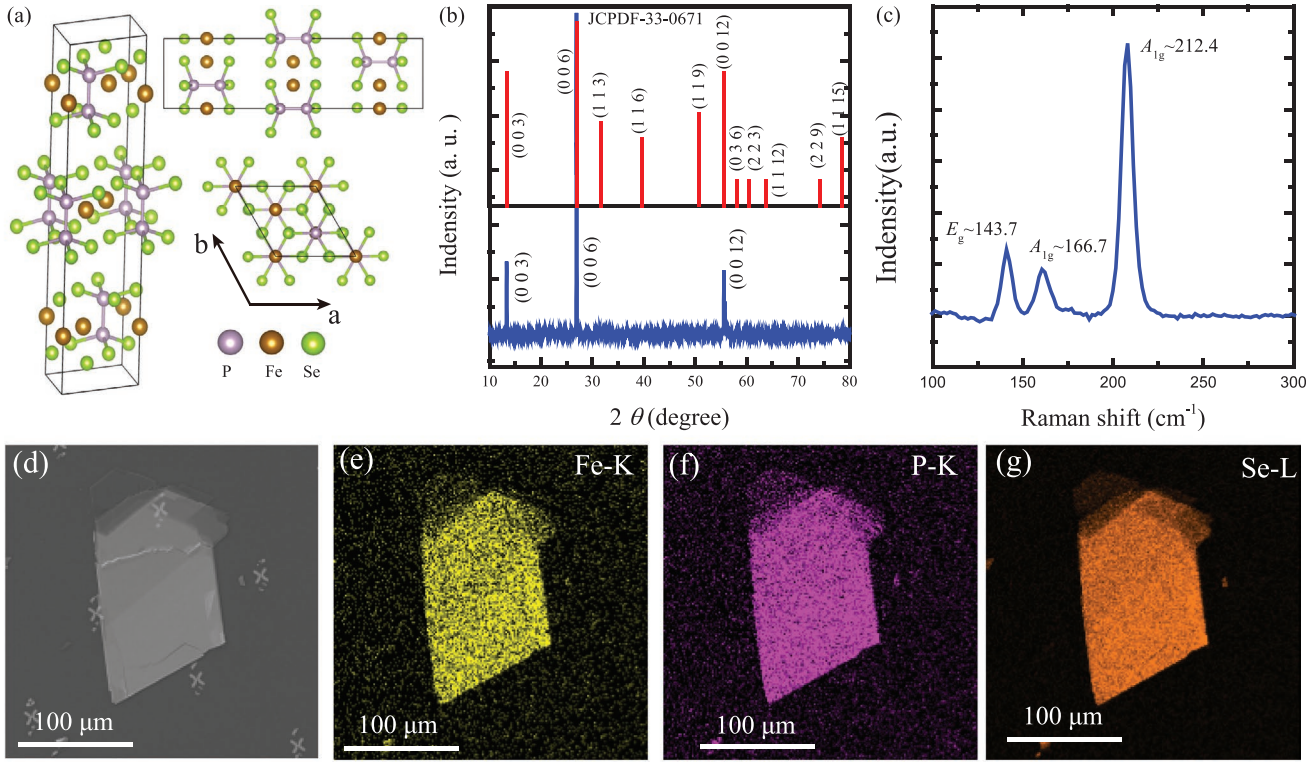

Figure 1. Characterization of the $FePSe_3$ single crystal. a) Schematic images of the $FePSe_3$ atomic structure. b) XRD diffraction pattern of a multilayer $FePSe_3$ flake. c) Raman spectrum of a multilayer $FePSe_3$ flake. d–g) EDS mapping images of a $FePSe_3$ flake, exhibiting the uniform distribution of Fe, P, and Se elements.

2D semiconductor with indirect energy of 1.3 eV,[20] corresponding to the near-infrared range. Broadband photodetection from visible to shortwave infrared (SWIR) based on $FePSe_3$ thin flacks was demonstrated.[21,22] However, UV detectors based on MPX_3 suffer from low photoresponsivity, slow response speed, limited specific detectivity, and a narrow spectral response range. Broadening the detection window requires tuning down the bandgap to extend the absorption band edge to the infrared spectrum. Using the heterostructures based on narrow bandgap semiconductors Ge,[23] $PdSe_2$,[24–26] and $PtSe_2$,[27] and $PtTe_2$,[28] the ultra-broadband photoresponse was demonstrated. The typical n-type 2D layered material MoS_2 and perovskite heterocrystals were widely investigated and exhibited high-performance photoresponse in the visible range.[29–32] 2D van der Waals (vdW) *p-n* junction can be obtained based on $FePS_3$ and MoS_2.

Here, we report a highly sensitive ultra-broadband photodetector based on a $FePSe_3/MoS_2$ vdW heterostructure. The rectification behavior was observed with a rectification ratio up to 10^2. High photoresponsivity up to 33, 600 A W^{-1} and EQE up to 1.57×10^7% were demonstrated in SBUV 265 nm at a bias of 1 V. The excellent performance in the UV range includes a NEP extremely low at 7.1×10^{-16} W Hz$^{-1/2}$ and a detectivity up to 1.51×10^{13} Jones. Notably, the device exhibits an ultra-broadband photoresponse from deep UV 265 nm to LWIR 10.6 μm. The photoresponsivity up to 0.12 A W^{-1} and a detectivity of 4.92×10^8 Jones were demonstrated at 10.6 μm in ambient air. The performance at room temperature in the mid-wave infrared (MWIR) range is comparable to that of a commercially available PbSe detector, and in LWIR, it is better than that of the bolometers.

2. Results and Discussion

The $FePSe_3$ (FPS) single crystal growth was carried out in a two-temperature zone tube furnace using the chemical vapor transport (CVT) method. High-purity powders Fe (200 mesh 99+%, Alfa Aesar), Se (99.9%, Alfa Aesar), and red phosphorus (100 mesh, 99%, Alfa Aesar) were fully mixed in an agate mortar at a stoichiometric ratio of 1: 1: 3.15, which was carried out in an inert gas-filled glove box. A slight excess of Se is used as a transport medium. Then, the mixed powder was pressed into the tablet and sealed in an evacuated quartz tube. The quartz tube was placed in a two-zone tube furnace. The sour end was kept at 750 °C and the growth end was kept at 700 °C for six days. Then, the furnace was switched off and cooled to room temperature. The $FePSe_3$ single crystal was obtained. The crystal structures of the MPX_3 family have the monoclinic C2/m space group,[2] **Figure 1**a shows a schematic of the $FePSe_3$ crystal structure. In the monolayer crystal structure of $FePSe_3$, each Se atom is bound to two Fe atoms and one P atom, and P atoms are tetrahedrally bound with three Se atoms and one P atom forming a bipyramid $[P_2Se_6]^{4-}$ unit (side view). The $[P_2Se_6]^{4-}$ unit wrapped in the center of six nearby Fe atoms forms a honeycomb structure (top view). The layered structure is easily exfoliated into

thin flacks. The X-ray diffraction (XRD) pattern of the as-synthesized $FePSe_3$ single-crystal flake was measured, as shown in the bottom panel of Figure 1b. Three main peaks (0 0 3), (0 0 6), and (0 0 12) are located at $2\theta = 13.38°$, 27.01°, and 55.65°, respectively, which match very well with the reported No. 33–0671 JCPDF card,[33,34] as shown in the top panel of Figure 1b. The Raman spectrum of the prepared $FePSe_3$ is shown in Figure 1c. Three characteristic Raman peaks at 143.7, 166.7, and 212.4 cm^{-1} are related to the vibration of $E_g(\nu 12)$, A_{1g} ($\nu 2$), and A_{1g} ($\nu 1$), respectively, and the vibration of the P-Se bound in the P_2Se_6 unit, which is consistent with previous reports.[21,22,33] The element mapping images of the prepared $FePSe_3$ were measured by energy-dispersive X-ray spectroscopy (EDS), as shown in Figures 1d–g. The EDS spectrum is presented in Figure S1 (Supporting Information). The atomic ratio of Fe: P: Se is 21.9: 21.7: 56.3, as shown in the inset of Figure S1 ((Supporting Information)), which is very close to 1: 1: 3.

To examine the electronic transport properties of $FePSe_3$, we exfoliated FPS onto a Si/SiO_2 substrate and fabricated a $FePSe_3$ field-effect transistor (FET). The transfer curve of a $FePSe_3$ FET device at a bias of 2 V is plotted in Figure S2a (Supporting Information). The optical image of the device is presented in the inset of Figure S2a (Supporting Information). The typical *p*-type semiconductor transport behavior is consistent with the literature.[20] The mobility of $FePSe_3$ could be calculated using $\mu = L/(WC_gV_{ds})$ (dI_{ds}/dV_g), where L and W are the channel length and width, respectively, and C_g = 11.5 nF cm^{-2} is the capacitance per unit area of the 300 nm SiO_2. The mobility of $FePSe_3$ is $\approx 2.5 \times 10^{-3}$ cm^2 V^{-1} s^{-1}, which is slightly higher than the previously reported value of 1.62×10^{-3} cm^2 V^{-1} s^{-1}.[21] The *I–V* curves at dark and under various incident light powers of SBUV 265 nm light are presented in Figure S2b (Supporting Information). The temporal photoresponse of the $FePSe_3$ FET device under various incident light powers at a bias of 2 V is shown in Figure S2c (Supporting Information). The extracted illumination power dependence R and EQE are presented in Figure S2d (Supporting Information). A high photoresponsivity of 29.1 A W^{-1} and corresponding EQE of 13569.8% was realized at 0.04 nW. As the incident light power increased, the R and EQE showed a decreasing tendency. As the light power increased to 0.46 nW, the R and EQE decreased to 7.7 A W^{-1} and 3617.1%.

Then, we fabricated the $FePSe_3/MoS_2$ vdW heterodiode. A schematic diagram of the $FePSe_3/MoS_2$ vdW heterodiode is presented in **Figure 2**a. A bottom mirror electrode is used for enhancing light absorption and efficient light absorption. Figure 2b presents the optical image of a typical $FePSe_3/MoS_2$ vdW device. The thickness of the heterodiode device was examined by atomic force microscopy (AFM). The AFM image is presented in Figure S3a (Supporting Information). The thicknesses of $FePSe_3$ and MoS_2 are 17.4 and 8.1 nm, respectively, as shown in Figure S3b,c (Supporting Information). Then, we examine the optoelectric properties of the device. A few optical microscope photographs of the $FePSe_3/MoS_2$ vdW device are presented in Figure S4 (Supporting Information). As shown in Figure 2c, the output curve of the heterodiode with a rectification ratio of 10^2 is obtained. The semilogarithmic plot of the output curve is shown in the inset of Figure 2c. Form the generalized diode equation of $I = I_0$ [exp(q V_{ds}/n k_B T)–1], where I_0 is the reverse saturation current and n is the ideality factor.[35] From the *I–V* curve, the ideality Factor n = 1.1 was obtained. An ideality factor very close to 1 indicates that the heterodiode is near ideal diode behavior[36,37] with a high-quality interface.

To explore the photoresponse in the SBUV range, we measured the $FePSe_3/MoS_2$ vdW *I–V* curves by varying the incident light power, as shown in Figure 2d. The incident light source is a 265 nm UV–light-emitting diode (LED). The device was placed in the position under the LED 2 mm without the lens. To evaluate the performance of the device, the photoresponsivity, the ratio of photocurrent to incident light power $R = I_P/P$, and external quantum efficiency (EQE = h c R/e λ) were calculated. Figure 2e shows the R and EQE versus light power at a bias of 4 V of SBUV 265 nm light. An R of up to 33 600 A W^{-1} and EQE of 1.57×10^7% were demonstrated at 0.23 nW. In the low-power region, R and EQE exhibit a saturated tendency. As the incident light power increased, the R and EQE decreased to 11 700 A W^{-1} and 5.74×10^6%, respectively. The EQE is much higher than 100%, indicating that the photo gain (G) plays an important role in this device. Photo gain is defined as the ratio of photocarrier lifetime (τ_l) to transport time (τ_t) $G = \tau_l/\tau_t$, where $\tau_t = L^2/\mu V_{ds}$. The photo gain can be expressed as $G = \tau_l \mu V_{ds}/L^2$. The R and EQE at a bias of 1 V are presented in Figure S5a (Supporting Information). The R of 1551.7 A W^{-1} and EQE of 7.26×10^5% are obtained. The photovoltaic response of the vdW heterodiode under SBUV 265 nm is plotted in Figure 2f. The R of 0.092 A W^{-1} and a corresponding EQE of 43.2% was achieved. The photoresponse of the device in a near-ultraviolet (NUV) range of 365 nm was investigated. The R and EQE at a bias of 1 V as a function of incident light power are presented in Figure S5b (Supporting Information). The R of 360 A W^{-1} and EQE of 1.22×10^5% are obtained at 1.1 nW of 365 nm UV light. To evaluate the performance of the $FePSe_3/MoS_2$ vdW heterodiode in the UV range, a comparison with other materials regarding the photoresponsivity and wavelength is presented in Figure S5c (Supporting Information). In the near UV region, the R of our device is slightly higher than that of In_2Se_3 395 A W^{-1},[38] $MnPS_3$ 288 A W^{-1},[5] $Ga_2In_4S_9$ 111.9 A W^{-1},[9] and Ga_2S_3 of 61.3 A W^{-1}.[39] While in the solar-blind spectrum (230–280 nm), the R of 33 600 A W^{-1} for the $FePSe_3/MoS_2$ vdW photodetector is three orders higher than that of the observation of the high on BiOCl of 35.7 A W^{-1}[15] for other 2D materials. These results indicate that the $FePSe_3/MoS_2$ vdW photodetector has an excellent performance in the SBUV region. The key parameters of UV photodetectors are summarized in the supplementary information in Table S1 (Supporting Information). In the visible range, the photoresponse under 520 and 637 nm lasers were investigated. The *I–V* curves with and without illumination (520 nm laser) are plotted in Figure S6a (Supporting Information). Then, the extracted photoresponsivity and EQE versus light power are presented in Figure S6b (Supporting Information). An R of 2456.8 A W^{-1} and a corresponding EQE of 5.8×10^5% are obtained at 4.0 nW. **Figure 3**a presents the semilogarithmic plot of *I–V* curves of a typical device under a 637 nm laser. The light power varied from 100 nW to 15.1 μW. To examine the performance of the device, the temporal response was measured at a bias of 1 V, as shown in Figure 3b. As the light incident on the device, the current increased sharply. Few cycles switch off the light, and

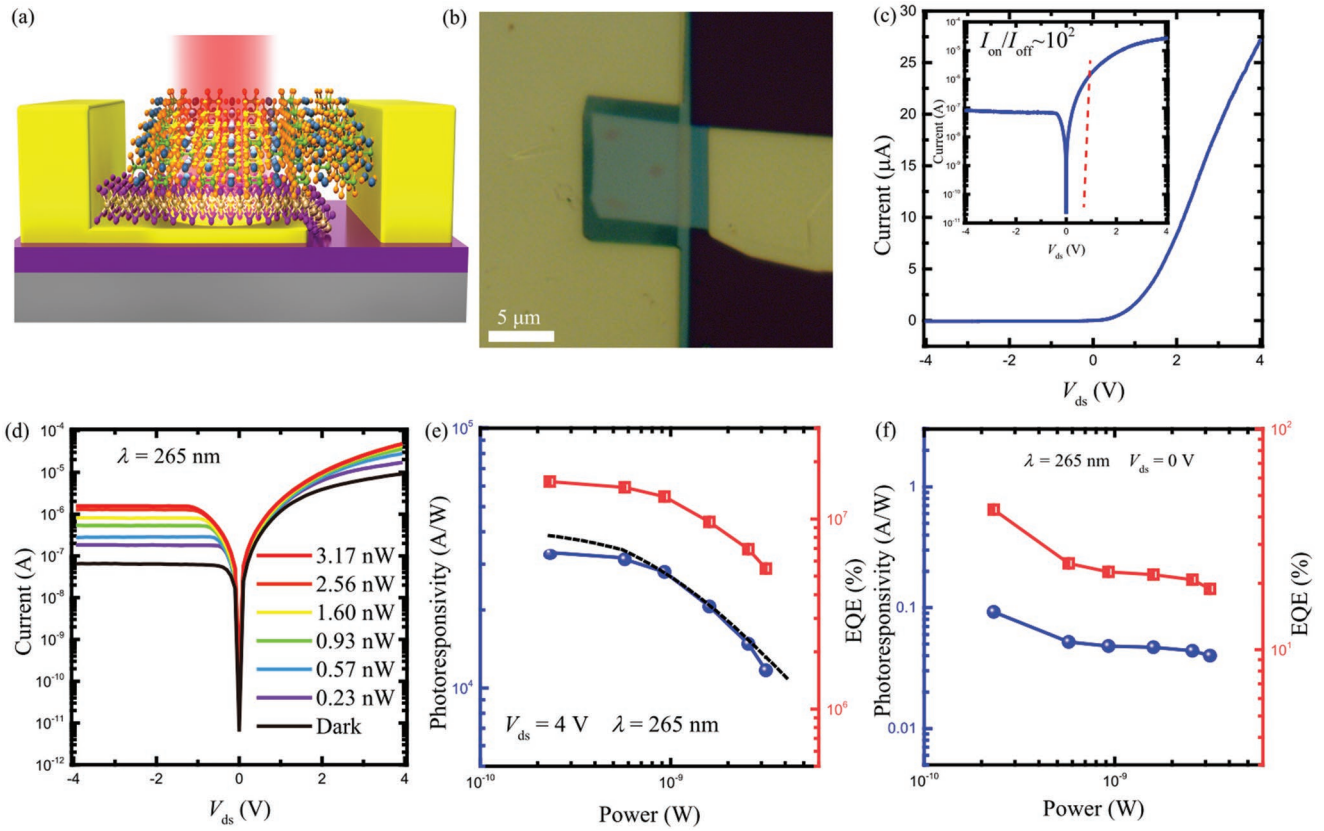

Figure 2. The photoresponse of a typical $FePSe_3/MoS_2$ vdW heterodiode in the SBUV range. a) Schematic image of the $FePSe_3/MoS_2$ vdW heterodiode photodetector. b) Optical microscope image of the $FePSe_3/MoS_2$ heterodiode device. c) I_{ds}–V_{ds} curve of the $FePSe_3/MoS_2$ vdW heterodiode. Inset: the semilogarithmic plot of the I_{ds}–V_{ds} curve. d) The semilogarithmic plot of I_{ds}–V_{ds} curves with and without the illumination of 265 nm light. e) Incident light power-dependent photoresponsivity R and EQE of a typical device under SBUV 265 nm irradiation at a bias of V_{ds} = 4 V. f) Incident light power dependence photovoltaic R and EQE of a typical $FePSe_3/MoS_2$ vdW heterodiode device under solar-blind UV 265 nm LED lamp.

the photocurrent shows good repeatability. Figure 3c shows the extracted R and EQE at a bias of 4 V. In the low-power region, the R of 67.6 A W^{-1} was obtained and exhibited a saturated tendency, which was observed frequently in 2D material photodetectors due to the existence of the trap centers. The corresponding EQE of 13 173% is realized at 7.3 nW. The time-resolved photoresponse under various light powers at –1 V is presented in Figure S6c (Supporting Information). The R and EQE of the 637 nm laser at a bias of 1 V are presented in Figure S6d (Supporting Information). At a low incident power of 7.3 nW, the R of 3.92 A W^{-1} and EQE of 764% is obtained. The incident power dependence photocurrent can be well described by the Hornbeck- Haynes model.[40,41]

$$I_p = q\eta\left(\frac{\tau_l}{\tau_t}\right)\frac{F}{1+F/F_0} \quad (1)$$

where, whereη is the light absorption efficiency, F and F_0 in units of s^{-1} are the photon absorption rates at unsaturated and saturated trap centers, respectively. Therefore, the photo responsivity can be obtained:

$$R = \frac{e\lambda\eta^2}{h\,c}\left(\frac{\tau_L}{\tau_T}\right)\frac{1}{1+F/F_0} \quad (2)$$

The incident light powers dependence R could be well fitted by Equation 2 as shown in Figures 2e and 3c, the black dashed lines. The rapid drop of the R from SBUV to the visible range 637 nm could be attributed to the that a remarkable higher photogain could be realized in a higher exciting photon and low incident light power density. As shown in Figure S7 (Supporting Information), at the low incident power density, most of the trap centers are empty. For higher energy photons, the electrons were pumped to higher energy states, which could be trapped by higher energy trap centers. After going through a lifetime of the trap state, the trapped electron could be re-trapped by another trap state before recombination. At this condition, a long lifetime τ_l could be realized and obtain a higher photogain $G = \tau_l/\tau_t$. Another important figure of merit, the response time, which is one of the most important figures of merit for photodetectors, is presented in Figure 3d. The rise time (from 10% to 90%) and decay time (from 90% to 10%) were 0.32 and 0.36 ms, respectively. This speed is much faster than that of other photodetectors of MPX_3, such as $MnPS_3$ of 340,[5] $NiPS_3$ of 17.5,[7] $FePS_3$ of 260,[8] and $FePSe_3$ of 183 ms.[21] Then, the photoresponses of MWIR and LWIR were examined. The time-resolved photoresponse under a 2611 nm laser at a bias of 1 V is presented in Figure S8a (Supporting Information). After fifteen cycles of light switching, the photoresponse

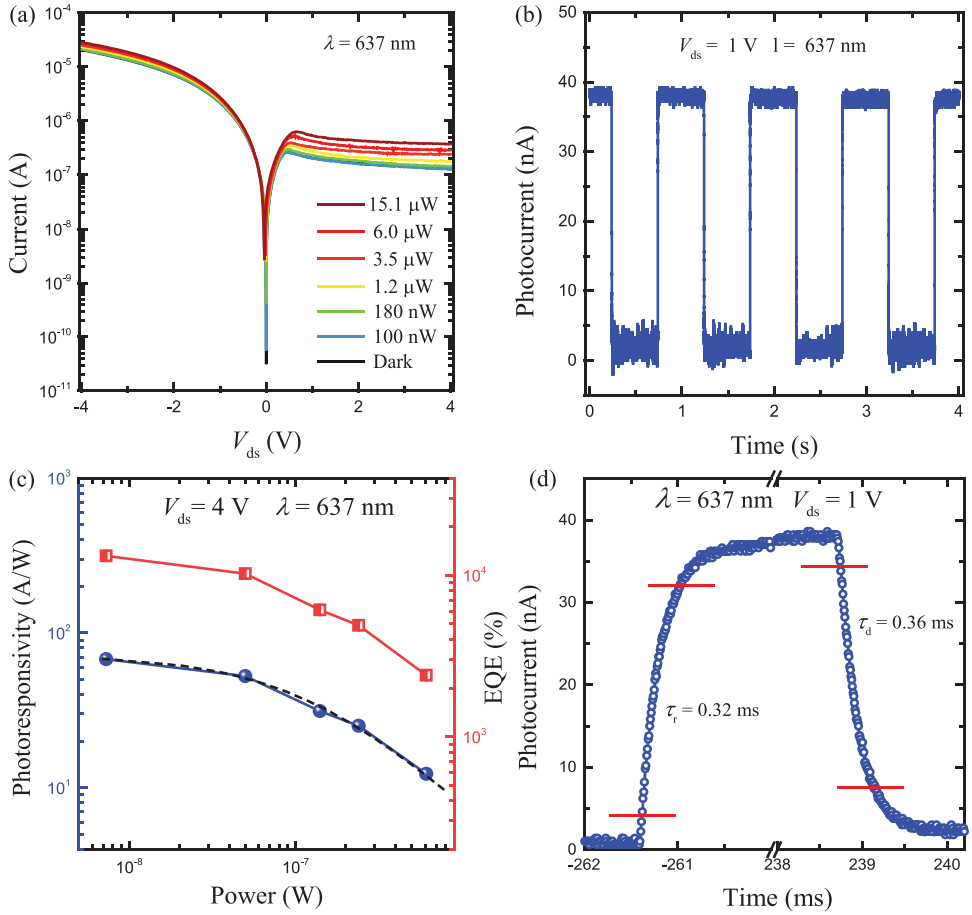

Figure 3. Wavelength dependence of the photoresponse of the $FePSe_3/MoS_2$ heterodiode. a) A semilogarithmic plot of *I*–*V* curves in the dark and with different powers of a 637 nm laser. b) Temporal photoresponse under a few cycles of the switch on/off the incident light. c) Incident light power dependence of the photoresponsivity *R* (left axis) and EQE (right axis) for a typical device versus illumination power under visible light of 637 nm irradiation. d) Response time of a typical $FePSe_3/MoS_2$ heterodiode device at a bias of 1 V. The rise-decay time was defined as the photocurrent increasing/decreasing from 10/90% to 90/10% of the stable photocurrent.

is fast and exhibits good repeatability. The temporal photoresponses of the 3403 nm lasers at a bias of 1 V with varying incident power are presented in Figure S8b (Supporting Information). Compared with the photoresponse at 2611 nm, the response speed in this range is slow. The light power dependence *R* and EQE are plotted in Figure S8c (Supporting Information). The *R* of 0.69 A W^{-1} and a corresponding EQE of 20.8% is obtained at 0.41 μW with a 3403 nm laser. We also examined the photoresponse in LWIR 10.6 μm. The time-resolved photoresponse of LWIR 10.6 μm laser for change incident light power at a bias of 4 V, as shown in **Figure 4**a,b shows the *R* and EQE versus incident LWIR 10.6 μm light power. The *R* of 1.09 A W^{-1} corresponding to an EQE of 12.8% is obtained under 0.33 μW illumination, indicating that this $FePSe_3/MoS_2$ vdW photodetector has an excellent LWIR response. As the incident light power increases, the *R* and EQE decrease slightly. The *R* dropped to 0.35 A W^{-1} as the power increased to 2.39 μW. Figure S8d (Supporting Information) summarizes the detection range of the 2D materials. The detection range of our detector is covered from SBUV to LWIR, which is much broader than other MPX_3 from SBUV to SWIR. Compared with narrow bandgap 2D materials, such as BP from visible to MWIR 3.39 μm[40] and using a vertical electrical field extending to 7.7 μm,[42] Te (VIS to MWIR),[43,44] B-AsP,[45] $PdSe_2$,[46] and $PtSe_2$[47] and graphene[48] from VIS to LWIR, this device exhibits excellent SBUV detection ability. The performance of UV detectors operating from the extreme ultraviolet (EUV) to NUV range, such as H-BN,[19] $Sr_2Nb_3O_{10}$,[10] SiAs,[49] GaS,[50] GaN,[11,51] Ga_2O_3,[52,53] KNb_3O_8,[17] and BiOCl.[15,16] The performance of UV detectors is summarized in Table S1 in the Supporting information.

Figure 4c presents the wavelength dependence of *R* and EQE at a bias of 1 V. The $FePSe_3/MoS_2$ vdW device exhibits a good response from SBUV to LWIR (0.265–10.6 μm). In the SBUV range, the *R* of 1551.7 A W^{-1} and corresponding EQE of 7.2 × 10^5% were demonstrated. In the visible range, *R* drops to 18 A W^{-1}, and in the MWIR, *R* ranges from 0.2 to 0.7 A W^{-1}. As the wavelength was extended to LWIR 10.6, the *R* of 0.12 A W^{-1} and EQE of 1.42% was obtained. To evaluate the sensitivity of the device, the noise equivalent power (NEP) and specific detectivity *D** were calculated. We measured the current noise power spectra at different biases, as shown in Figure S8e (Supporting Information). Figure 4d presents the wavelength dependence of EQE and *D** at a bias of V_{ds} = 1 V.

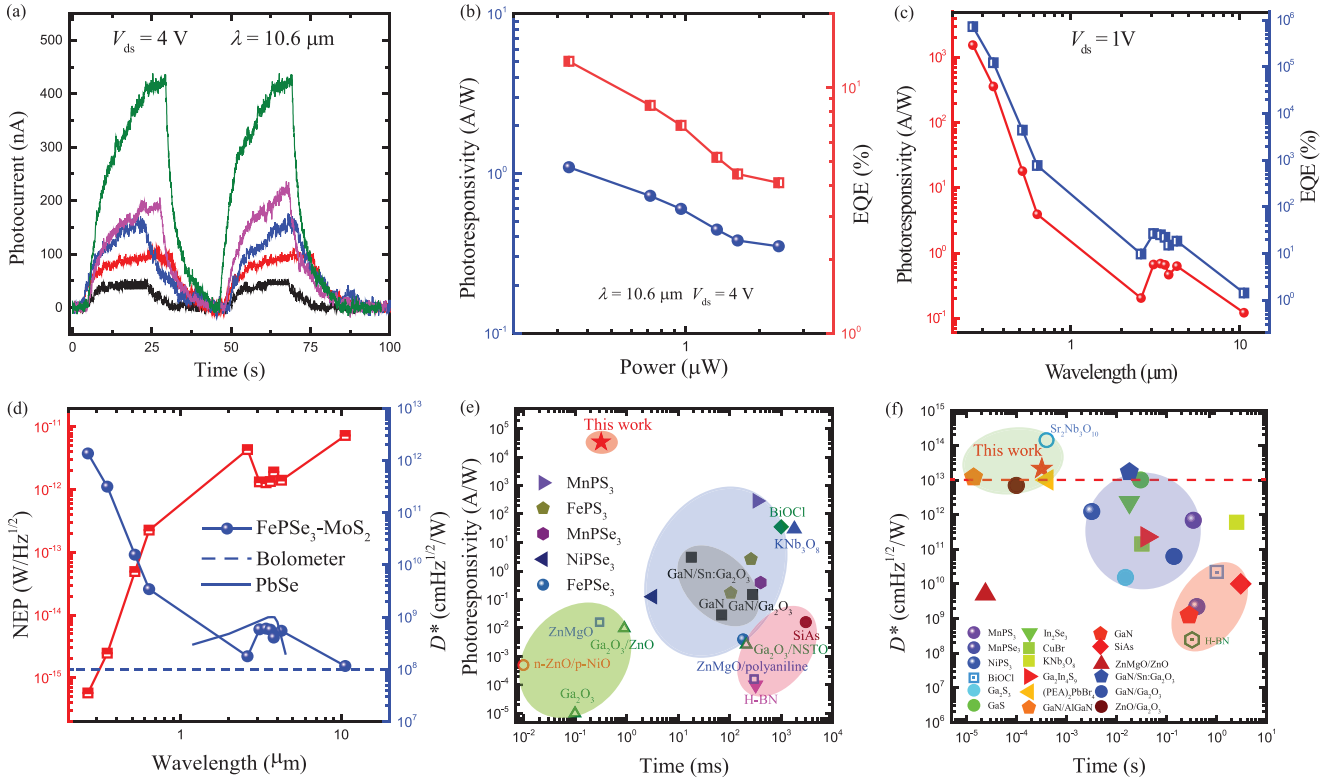

Figure 4. Wavelength dependence *R* and *D** of the $FePSe_3/MoS_2$ heterodiode. a) Temporal photoresponse of the LWIR 10.6 μm laser at a bias of 4 V in ambient conditions. b) Incident light power dependence *R* and EQE at a bias of 4 V under a 10.6 μm laser. c) Photoresponsivity and EQE as a function of wavelength of the $FePSe_3/MoS_2$ heterodiode at a bias of 1 V. d) Left axis: the NEP versus wavelength at a bias of 1 V, and the right axis: the wavelength dependence *D** of the $FePSe_3/MoS_2$ heterodiode compared with the commercially available PbSe and bolometer detectors. e) and f) Comparison of the UV photodetector's photoresponsivity versus response time and specific detectivity versus response time based on 2D materials and other wide bandgap semiconductors, respectively.

The NEP could be obtained by the formula NEP = i_n/R. The root-mean-square noise current$<i_n^2>^{1/2}$ = 8.85 × 10^{-13} A $Hz^{-1/2}$ was obtained at a bias of 1 V. The value is consistent with the short noise, $<i_n^2>^{1/2} = (2eI_{dark})^{1/2}$ = 7.2 × 10^{-13} A $Hz^{-1/2}$ with I_{dark} = 1.62 × 10^{-6} A. The NEP of 5.7 × 10^{-16} W $Hz^{-1/2}$ was demonstrated in the SBUV range. In the MWIR range, the NEP was lower than 4.3 × 10^{-12} W $Hz^{-1/2}$, and in LWIR 10.6 μm, the NEP was 7.3 × 10^{-12} W $Hz^{-1/2}$. In the full operation spectra range, the $FePSe_3/MoS_2$ vdW device exhibits excellent performance. The specific detectivity, which represents the detection limit of a photodetector, can be calculated by $D^* = (AB)^{1/2}/NEP$, where A is the effective area of the device. At a bias of 1 V, a *D** of 1.34 × 10^{12} cm $Hz^{1/2}$ W^{-1} is obtained in SBUV 265 nm. In the MWIR and LWIR, *D** is 1.77 × 10^8 cm $Hz^{1/2}$ W^{-1} and 1.05 × 10^8 cm $Hz^{1/2}$ W^{-1}, respectively. The *D** in MWIR is compared with a commercially available PbSe detector, and in the LWIR, the *D** is larger than the bolometer of 10^8 cm $Hz^{1/2}$ W^{-1}. Notably, at a bias of 4 V, the root-mean-square noise current$<i_n^2>^{1/2}$ = 2.4 × 10^{-12} A $Hz^{-1/2}$. The *D** is up to 1.51 × 10^{13} cm $Hz^{1/2}$ W^{-1} at the *R* = 33 600 A W^{-1} of SBUV 265 nm. Figure 4e,f summarizes the *R* and *D** versus response time of the 2D material UV photodetectors. In Figure 4e, the *R* of our $FePSe_3/MoS_2$ vdW heterodiode device is much higher than that of other UV photodetectors based on 2D materials and other WBSs. The response time of our device is much faster than other MPX_3 (3–400 ms) marked by a blue ellipse and GaN/Ga_2O_3 heterostructures[54,55] marked by a grey ellipse. The fast response speed with low *R* of ZnMgO,[56] ZnO/NiO,[57] Ga_2O_3/ZnO,[53,58] and Ga_2O_3 are marked by a green ellipse, and the slow response speed and low *R* of SiAs,[49] H-BN[19] and polyaniline/ZnMgO bilayer[56] are marked by a pink ellipse. The higher performance in photoresponsivity could be attributed to the vertical vdW heterostructure device structure placed on a bottom mirror electrode and the high quality of the device with a clean interface. The bottom mirror electrode plays an important role not only in enhancing the light absorption but also in shortening the photocarriers' lateral transport distance, thereby reducing the photocarriers' transport time τ_t. The high efficiency of photocarriers collection could reduce the photocarriers recombination and realize high photo gain. In Figure 4f, *D** is higher than 10^{13} cm $Hz^{1/2}$ W^{-1}, and the fast response speed (<1 ms) is marked by a green ellipse, including $Sr_2Nb_3O_{10}$ of 1.40 × 10^{14} cm $Hz^{1/2}$ W^{-1},[10] GaN/AlGaN, $(PEA)_2PbBr_4$ perovskite 10^{13} cm $Hz^{1/2}$ W^{-1},[59] and α-Ga_2O_3/ZnO of 9.66 × 10^{12} cm $Hz^{1/2}$ W.[53] The relatively high *D** with (10^{10}–10^{12} cm $Hz^{1/2}$ W^{-1}) and mid-speed (1–300 ms) are marked by a blue circle, and low *D** (<10^{10} cm $Hz^{1/2}$ W^{-1}) and low speed are marked by a red ellipse. The band alignment of the $FePSe_3/MoS_2$ vdW heterodiode is presented in Figure S9 (Supporting Information). The work function of $FePSe_3$ is ≈5.16 eV,[60] and

MoS_2 is 5.05 eV[61] respectively. The type II band alignment for $FePSe_3/MoS_2$ vdW heterostructure, the absorption spectra range of interlayer light absorption ($h\nu_3$) much broader than that of the for $FePSe_3$ ($h\nu_1$) and MoS_2 ($h\nu_2$). In the MWIR and LWIR, the photo-bolometer effect[62] may play an important role in photoresponse in these $FePSe_3/MoS_2$ vdW heterodiode devices. Notably, the device is very stable in the ambient air. The device fabrication process and the optoelectronic performance measurement were carried out in ambient air. As shown in Figure S10 (Supporting Information), the device was exposed to the air for more than 4 months, and the photoresponse did not show any decline.

In summary, we report an ultra-broadband $FePSe_3/MoS_2$ vdW heterodiode photodetector. The operation spectrum covers from SBUV to LWIR (0.265–10.6 µm). The high photoresponsivity up to 33 600 A W and extremely low NEP of $\approx 7.1 \times 10^{-17}$ W $Hz^{-1/2}$ and high D^* of 1.51×10^{13} cm $Hz^{1/2}$ W^{-1} were demonstrated in the SBUV range. The performance in this range is remarkable compared with that of state-of-the-art SBUV photodetectors. Notably, the device also exhibits excellent room temperature MWIR and LWIR detection abilities. A D^* of 6.01×10^8 cm $Hz^{1/2}$ W^{-1} in the MWIR region and 4.92×10^8 cm $Hz^{1/2}$ W^{-1} in LWIR 10.6 µm was achieved in ambient air. Our results reveal that the $FePSe_3/MoS_2$ heterodiode is a promising candidate for high-performance solar-blind UV detectors and ultra-broadband uncooled mid-infrared detection.

3. Experimental Section

Device Fabrication: The bottom mirror electrodes were patterned using electron-beam lithography and then using the electron-beam evaporation deposition of 5 nm Cr and 25 nm Au on a low resistance Si substrate with 300 nm SiO_2. The $FePSe_3$ and MoS_2 flakes were prepared using a scotch tape exfoliation method and then transferred to a pre-deposited bottom electrode. The top contact metal electrode of 5 nm Cr and 50 nm Au was then evaporated using thermal evaporation.

Characterization Methods: The crystal structure of $FePSe_3$ was characterized by XRD. The element distribution mapping of $FePSe_3$ was measured using energy-dispersive X-ray spectroscopy (EDS). The thicknesses of the $FePSe_3$ and MoS_2 flakes were checked by AFM (HITACHI, AFM 5500M). Raman spectra were measured using a 532 nm laser as an exciting light by the Renishaw inVia-Reflex system.

Electrical and Photoresponse Measurements: The photocurrent and electrical transport measurements were carried out in ambient air. A dual-channel digital source meter (Keithley 2636B) was used as a voltage source and ampere meter. The ultraviolet light-emitting diode 265 and 365 nm LED were used as UV–light sources without focus. A homemade wavelength-tuneable multichannel MWIR laser (2.5–4.2 µm) and a CO_2 LWIR laser of 10.6 µm was used to study the MWIR and LWIR performance of those detectors. The diameter of the MWIR laser and LWIR beam is 3 mm. From visible to near-infrared (520 to 1650 nm), the laser was focused on the device using a 20× objective lens. Current noise density spectra were measured using a homemade noise spectrum analyzer (NC300). The device was placed in a shielded metal box with a 100 kHz measure bandwidth at various bias voltages in ambient air.

Supporting Information

Supporting Information is available from the Wiley Online Library or from the author.

Acknowledgements

This work was supported by the National Natural Science Foundation of China (Grant Nos. 61975224 and 62004207, 12074002), University Synergy Innovation Program of Anhui Province (Grant No. GXXT-2020-050), Fund of Anhui Provincial Natural Science Foundation (Grant No. 2008085MF206), Recruitment Program for Leading Talent Team of Anhui Province 2020, State Key Laboratory of Luminescence and Applications (Grant No. SKLA-2021-03), and Open Fund of Infrared and Low-Temperature Plasma Key Laboratory of Anhui Province (Grant No. IRKL2022KF03).

Conflict of Interest

The authors declare no conflict of interest.

Author contributions

M.L., Z.S., and R.W. contributed equally to this work. M.L. and L.S. conceived the project and designed the experiments. M.L., Z.S., R.W., and Q.D. performed device fabrication and characterization. M.L., Z.S., F.W., J.H., and L.S. performed data analysis and interpretation. M.L., Z.S., R.W., and L.S. co-wrote the paper, and all authors contributed to the discussion and preparation of the manuscript.

Data Availability Statement

The data that support the findings of this study are available from the corresponding author upon reasonable request.

Keywords

$FePSe_3$, heterojunctions, photodetectors, solar-blind ultraviolet, 2D materials

Received: April 14, 2022
Revised: May 28, 2022
Published online: June 15, 2022

[1] R. Samal, G. Sanyal, B. Chakraborty, C. S. Rout, *J. Mater. Chem. A* **2021**, *9*, 2560.
[2] K. Du, X. Wang, Y. Liu, P. Hu, M. I. B. Utama, C. K. Gan, Q. Xiong, C. Kloc, *ACS Nano* **2016**, *10*, 1738.
[3] M. Long, P. Wang, H. Fang, W. Hu, *Adv. Funct. Mater.* **2019**, *29*, 1803807.
[4] C. Xie, X. T. Lu, X. W. Tong, Z. X. Zhang, F. X. Liang, L. Liang, L. B. Luo, Y. C. Wu, *Adv. Funct. Mater.* **2019**, *29*, 1806006.
[5] R. Kumar, R. N. Jenjeti, M. P. Austeria, S. Sampath, *J. Mater. Chem. C* **2019**, *7*, 324.
[6] X. Han, P. Song, J. Xing, Z. Chen, D. Li, G. Xu, X. Zhao, F. Ma, D. Rong, Y. Shi, M. R. Islam, K. Liu, Y. Huang, *ACS Appl. Mater. Interfaces* **2021**, *13*, 2836.
[7] J. Chu, F. Wang, L. Yin, L. Lei, C. Yan, F. Wang, Y. Wen, Z. Wang, C. Jiang, L. Feng, J. Xiong, Y. Li, J. He, *Adv. Funct. Mater.* **2017**, *27*, 1701342.
[8] M. Ramos, F. Carrascoso, R. Frisenda, P. Gant, S. Manas-Valero, D. L. Esteras, J. J. Baldov, E. Coronado, A. Castellanos-Gomez, M. R. Calvo, *NPJ 2D Mater. Appl.* **2021**, *5*, 19.
[9] F. Wang, T. Gao, Q. Zhang, Z. Hu, B. Jin, L. Li, X. Zhou, H. Li, G. Van Tendeloo, T. Zhai, *Adv. Mater.* **2019**, *31*, 1806306.

[10] S. Li, Y. Zhang, W. Yang, H. Liu, X. Fang, *Adv. Mater.* **2019**, *32*, 1905443.
[11] A. Gundimeda, S. Krishna, N. Aggarwal, A. Sharma, N. D. Sharma, K. K. Maurya, S. Husale, G. Gupta, *Appl. Phys. Lett.* **2017**, *110*, 103507.
[12] X. Fang, Z. Wei, Y. Yang, R. Chen, Y. Li, J. Tang, D. Fang, H. Jia, D. Wang, J. Fan, X. Ma, B. Yao, X. Wang, *ACS Appl. Mater. Interfaces* **2016**, *8*, 1661.
[13] G. Wolfowicz, C. P. Anderson, A. L. Yeats, S. J. Whiteley, J. Niklas, O. G. Poluektov, F. J. Heremans, D. D. Awschalom, *Nat. Commun.* **2017**, *8*, 1876.
[14] S. Oh, C. Kim, J. Kim, *ACS Photonics* **2018**, *5*, 1123.
[15] W. Han, C. Li, S. Yang, P. Luo, F. Wang, X. Feng, K. Liu, K. Pei, Y. Li, H. Li, L. Li, Y. Gao, T. Zhai, *Small* **2020**, *16*, 2000228.
[16] L. Kang, X. Yu, X. Zhao, Q. Ouyang, J. Di, M. Xu, D. Tian, W. Gan, C. C. I. Ang, S. Ning, Q. Fu, J. Zhou, R. G. Kutty, Y. Deng, P. Song, Q. Zeng, S. J. Pennycook, J. Shen, K. Yong, Z. Liu, *Info Mat* **2020**, *2*, 593.
[17] Y. Ping, H. Long, H. Liu, C. Chen, N. Zhang, H. Jing, J. Lu, Y. Zhao, Z. Yang, W. Li, F. Ma, X. Fang, Z. Wei, H. Xu, *Adv. Funct. Mater.* **2022**, 2111673.
[18] C. Gong, J. Chu, C. Yin, C. Yan, X. Hu, S. Qian, Y. Hu, K. Hu, J. Huang, H. Wang, Y. Wang, P. Wangyang, T. Lei, L. Dai, C. Wu, B. Chen, C. Li, M. Liao, T. Zhai, J. Xiong, *Adv. Mater.* **2019**, *31*, 1903580.
[19] H. Liu, J. Meng, X. Zhang, Y. Chen, Z. Yin, D. Wang, Y. Wang, J. You, M. Gao, P. Jin, *Nanoscale* **2018**, *10*, 5559.
[20] A. L. O. O. Levy, *J. Solid State Chemistry* **1987**, *72*, 316.
[21] T. Xu, M. Luo, N. Shen, Y. Yu, Z. Wang, Z. Cui, J. Qin, F. Liang, Y. Chen, Y. Zhou, F. Zhong, M. Peng, M. Zubair, N. Li, J. Miao, W. Lu, C. Yu, W. Hu, *Adv. Electron. Mater.* **2021**, 2100207.
[22] A. Li, Y. Ge, Y. Gan, Y. L. Ren, Y. He, Q. Chen, P. Wang, K. Zhang, S. A. Yang, J. Z. Wu, R. Chen, L. Zhang, Y. Gong, *Adv. Mater. Interfaces* **2021**, *8*, 2100491.
[23] D. Wu, J. Guo, C. Wang, X. Ren, Y. Chen, P. Lin, L. Zeng, Z. Shi, X. J. Li, C. Shan, J. Jie, **2021**, *15*, 10119.
[24] L. H. Zeng, Q. M. Chen, Z. X. Zhang, D. Wu, H. Yuan, Y. Y. Li, W. Qarony, S. P. Lau, L. B. Luo, Y. H. Tsang, *Adv. Sci.* **2019**, *6*, 1901134.
[25] L. Zeng, D. Wu, S. Lin, C. Xie, H. Yuan, W. Lu, S. P. Lau, Y. Chai, L. Luo, Z. Li, Y. H. Tsang, *Adv. Funct. Mater.* **2019**, *29*, 1806878.
[26] D. Wu, J. Guo, J. Du, C. Xia, L. Zeng, Y. Tian, Z. Shi, Y. Tian, X. J. Li, Y. H. Tsang, J. Jie, *ACS Nano* **2019**, *13*, 9907.
[27] L. Zeng, S. Lin, Z. Li, Z. Zhang, T. Zhang, C. Xie, C. Mak, Y. Chai, S. P. Lau, L. Luo, Y. H. Tsang, *Adv. Funct. Mater.* **2018**, *28*, 1705970.
[28] L. Zeng, D. Wu, J. Jie, X. Ren, X. Hu, S. P. Lau, Y. Chai, Y. H. Tsang, *Adv. Mater.* **2020**, *32*, 2004412.
[29] X. Liu, S. Hu, J. Luo, X. Li, J. Wu, D. Chi, K. Ang, W. Yu, Y. Cai, **2021**, *17*, 2100246.
[30] S. Feng, C. Liu, Q. Zhu, X. Su, W. Qian, Y. Sun, C. Wang, B. Li, M. Chen, L. Chen, W. Chen, L. Zhang, C. Zhen, F. Wang, W. Ren, L. Yin, X. Wang, H. Cheng, D. Sun, *Nat. Commun.* **2021**, *12*, 4094.
[31] P. Xiao, J. Mao, K. Ding, W. Luo, W. Hu, X. Zhang, X. Zhang, J. Jie, *Adv. Mater.* **2018**, *30*, 1801729.
[32] X. Zhang, T. Zhu, C. Ji, Y. Yao, J. Luo, *J. Am. Chem. Soc.* **2021**, *143*, 20802.
[33] D. Mukherjee, M. Austeria P, S. Sampath, *ACS Appl. Energy Mater* **2018**, *1*, 220.
[34] S. Otani, M. Shimada, F. Kanamaru, M. Koizumi, *Inorg. Chem.* **1980**, *19*, 1249.
[35] T. C. B. A. Jayakumar, *Elec. Lett.* **2000**, *36*, 291.
[36] Y. Jin, D. H. Keum, S. An, J. Kim, H. S. Lee, Y. H. Lee, *Adv. Mater.* **2015**, *27*, 5534.
[37] M. El-Tahchi, A. Khoury, M. De Labardonnie, P. Mialhe, F. Pelanchon, *Sol. Ener. Mater. & Sol. Cell.* **2000**, *62*, 393.
[38] R. B. Jacobs-Gedrim, M. Shanmugam, N. Jain, C. A. Durcan, M. T. Murphy, T. M. Murray, R. J. Matyi, R. L. I. Moore, B. Yu, *ACS Nano* **2014**, *8*, 514.
[39] N. Zhou, L. Gan, R. Yang, F. Wang, L. Li, Y. Chen, D. Li, T. Zhai, *ACS Nano* **2019**, *13*, 6297.
[40] Q. Guo, A. Pospischil, M. Bhuiyan, H. Jiang, H. Tian, D. Farmer, B. Deng, C. Li, S. Han, H. Wang, Q. Xia, T. Ma, T. Mueller, F. Xia, *Nano Lett.* **2016**, *16*, 4648.
[41] C. Soci, A. Zhang, B. Xiang, S. A. Dayeh, D. P. R. Aplin, J. Park, X. Y. Bao, Y. H. Lo, D. Wang, *Nano Lett.* **2007**, *7*, 1003.
[42] X. Chen, X. Lu, B. Deng, O. Sinai, Y. Shao, C. Li, S. Yuan, V. Tran, K. Watanabe, T. Taniguchi, D. Naveh, L. Yang, F. Xia, *Nat. Commun.* **2017**, *8*, 1672.
[43] M. Peng, R. Xie, Z. Wang, P. Wang, F. Wang, H. Ge, Y. Wang, F. Zhong, P. Wu, J. Ye, Q. Li, L. Zhang, X. Ge, Y. Ye, Y. Lei, W. Jiang, Z. Hu, F. Wu, X. Zhou, J. Miao, J. Wang, H. Yan, C. Shan, J. Dai, C. Chen, X. Chen, W. Lu, W. Hu, *Sci. Adv.* **2021**, *7*, f7358.
[44] L. Tong, X. Huang, P. Wang, L. Ye, M. Peng, L. An, Q. Sun, Y. Zhang, G. Yang, Z. Li, F. Zhong, F. Wang, Y. Wang, M. Motlag, W. Wu, G. J. Cheng, W. Hu, *Nat. Commun.* **2020**, *11*, 2308.
[45] M. Long, A. Gao, P. Wang, H. Xia, C. Ott, C. Pan, Y. Fu, E. Liu, X. Chen, W. Lu, T. Nilges, J. Xu, X. Wang, W. Hu, F. Miao, *Sci. Adv.* **2017**, *3*, e1700589.
[46] M. Long, Y. Wang, P. Wang, X. Zhou, H. Xia, C. Luo, S. Huang, G. Zhang, H. Yan, Z. Fan, X. Wu, X. Chen, W. Lu, W. Hu, *ACS Nano* **2019**, *13*, 2511.
[47] X. Yu, P. Yu, D. Wu, B. Singh, Q. Zeng, H. Lin, W. Zhou, J. Lin, K. Suenaga, Z. Liu, Q. J. Wang, *Nat. Commun.* **2018**, *9*, 1545.
[48] B. Y. Zhang, T. Liu, B. Meng, X. Li, G. Liang, X. Hu, Q. J. Wang, *Nat. Commun.* **2013**, *4*, 1811.
[49] D. Kim, K. Park, J. H. Lee, I. S. Kwon, I. H. Kwak, J. Park, *Small* **2021**, *17*, 2006310.
[50] P. Hu, L. Wang, M. Yoon, J. Zhang, W. Feng, X. Wang, Z. Wen, J. C. Idrobo, Y. Miyamoto, D. B. Geohegan, K. Xiao, *Nano Lett.* **2013**, *13*, 1649.
[51] M. A. Khan, J. N. Kuznia, D. T. Olson, J. M. Van Hove, M. Blasingame, L. F. Reitz, *Appl. Phys. Lett.* **1992**, *60*, 2917.
[52] X. Chen, K. Liu, Z. Zhang, C. Wang, B. Li, H. Zhao, D. Zhao, D. Shen, *ACS Appl. Mater. Interfaces* **2016**, *8*, 4185.
[53] X. Chen, Y. Xu, D. Zhou, S. Yang, F. Ren, H. Lu, K. Tang, S. Gu, R. Zhang, Y. Zheng, J. Ye, *ACS Appl. Mater. Interfaces* **2017**, *9*, 36997.
[54] D. Guo, Y. Su, H. Shi, P. Li, N. Zhao, J. Ye, S. Wang, A. Liu, Z. Chen, C. Li, W. Tang, *ACS Nano* **2018**, *12*, 12827.
[55] P. Li, H. Shi, K. Chen, D. Guo, W. Cui, Y. Zhi, S. Wang, Z. Wu, Z. Chen, W. Tang, *J. Mater. Chem. C* **2017**, *5*, 10562.
[56] H. Chen, P. Yu, Z. Zhang, F. Teng, L. Zheng, K. Hu, X. Fang, *Small* **2016**, *12*, 5809.
[57] P. Ni, C. Shan, S. Wang, X. Liu, D. Shen, *J. Mater. Chem. C* **2013**, *1*, 4445.
[58] B. Zhao, F. Wang, H. Chen, L. Zheng, L. Su, D. Zhao, X. Fang, *Adv. Funct. Mater.* **2017**, *27*, 1700264.
[59] Y. Zhang, Y. Liu, Z. Xu, H. Ye, Q. Li, M. Hu, Z. Yang, S. F. Liu, *J. Mater. Chem. C* **2019**, *7*, 1584.
[60] X. Zhang, X. Zhao, D. Wu, Y. Jing, Z. Zhou, *Adv. Sci.* **2016**, *3*, 1600062.
[61] L. Huang, N. Huo, Y. Li, H. Chen, J. Yang, Z. Wei, J. Li, S. Li, *J. Phys. Chem. Lett.* **2015**, *6*, 2483.
[62] Y. Wang, P. Wu, Z. Wang, M. Luo, F. Zhong, X. Ge, K. Zhang, M. Peng, Y. Ye, Q. Li, H. Ge, J. Ye, T. He, Y. Chen, T. Xu, C. Yu, Y. Wang, Z. Hu, X. Zhou, C. Shan, M. Long, P. Wang, P. Zhou, W. Hu, *Adv. Mater.* **2020**, *32*, 2005037.